Numerical and experimental studies of the flow around a partially submerged vertical cylinder

Valentin Ageorges, Jorge Peixinho, Gaële Perret, Ghislain Lartigue, Vincent Moureau

Numerical and experimental studies of the flow around a partially submerged vertical cylinder

V. Ageorges[a], J. Peixinho[a,b], G. Perret[a], G. Lartigue[c], V. Moureau[c]

a. Laboratoire Ondes et Milieux Complexes, (LOMC) CNRS et Université Le Havre Normandie
CNRS : UMR6294
valentin.ageorges@univ-lehavre.fr
b. Procédés et Ingénierie en Mécanique et Matériaux [Paris] (PIMM) Arts et Métiers, CNAM, Hésam Université, CNRS : UMR8006
c. COmplexe de Recherche Interprofessionnel en Aéothermochimie (CORIA), CNRS : UMR6614

Résumé :

L'écoulement et l'injection d'air autour d'un cylindre vertical partiellement immergé, en translation, est étudié expérimentalement et numériquement. Le régime d'écoulement est turbulent avec $15\,000 < Re < 60\,000$ *et* $0.4 < Fr < 1.7$*, où* Re *et* Fr *sont les nombres de Reynolds et de Froude adimensionnés à l'aide du diamètre* D *du cylindre. Une cavité à l'aval du cylindre est observée. L'objectif de ce travail est d'étudier les efforts de traînée, l'élévation de la surface libre et la vitesse critique à partir de laquelle il y a entraînement d'air. Un bon accord entre les expériences et les simulations a été trouvé, évaluant ainsi la profondeur de la cavité, le coefficient de traînée et la vitesse critique d'injection d'air.*

Abstract :

The flow around a vertical cylinder piercing the free-surface is studied experimentally and numerically. The cylinder has a free-end and the range of velocities are in the regime of turbulent wake with experiments and simulations carried out for $15\,000 < Re < 60\,000$ *and* $0.4 < Fr < 1.7$*, where* Re *and* Fr *are the Reynolds and Froude numbers based on the cylinder diameter* D*. A cavity downstream the cylinder is observed. The focus here is on drag force measurement, free-surface elevation, and critical velocity for air-entrainment. Specifically, a good agreement between experiments and simulations is obtained for the cavity depth, the drag coefficient and the critical velocity.*

Key words : Numerical simulations, Experiments, Free-surface, Air-entrainment

1 Introduction

The flow past ships [1], or an emerged body such as bridge pilar, is a fundamental, familiar and fascinating sight. Measurements and modelling of this simple flow can have relevance for the floating offshore structures and renewable energy systems [2]. The disordered motion of the free-surface in the wake of the cylinder is related to the drag experienced by the cylinder. The wake pattern is responsible for

the surface waves and the air-entrainment. Many experiments and numerical works have considered a single vertical cylinder geometry in fully submerged situation [3, 4, 5]. These works reported drag force measurements as a function of the Reynolds number, for cylindrical geometry in both numerical and experimental approach. The Reynolds number is defined as $Re = UD/\nu$ with U the velocity, D the cylinder diameter and ν the kinematic viscosity of the fluid. Few studies have been done taking into account the effect of the free-surface flow. This configuration modifies the pressure distribution around the cylinder. Numerically [6, 7], the flow around a wall mounted cylinder has shown the evolution of the drag coefficient C_D, the dimensionless drag force defined later, as well as the free-surface elevation for Re varying from 27 000 up to 458 000. They showed that the vorticity changes with depth along the cylinder and diminishes close to the free-surface. Experimental measurements [8] show a simular evolution of the local C_D near the free-surface. However, the evolution of C_D with Fr reached a maximum, as suggested by the experiments of Ducrocq [9], who investigated the behaviour of subcritical and supercritical flows for different slopes of a flume with $0.5 < Fr < 2.3$ and Re = 50 000. The Froude number is defined as $Fr = U/\sqrt{gD}$ with $g = 9.81\,\mathrm{m/s^2}$ the gravitational acceleration.

Experimentally, Keough *et al.* [10] analysed the evolution of the fountain height ahead of the cylinder. The authors concluded a dependency of the fountain height with Fr^2, and revealed that this evolution follows inviscid Bernoulli equation for small velocity. In addition, at the downstream side of the cylinder, the maximum cavity depth, $\mathcal{L}$, is believed to evolve with Fr^2 [8]. The cavity depth $\mathcal{L}$, sometimes called ventilated region, is schematised in figure 1(*b*). Furthermore, for large Re and Fr, free-surface is locally subjected to strong deformations behind the cylinder. In this situation, air bubbles are introduced in the liquid phase and Benusiglio [11] recently demonstrated a velocity threshold for air-entrainment in the cavity of a translating vertical cylinder.

Although, numerical simulations seem to reproduce well the drag on cylinder at such large Re, there is no data for strong free-surface deformations and air-entrainment phenomenon. Previous experiments have been performed for 1.4 < D < 16 cm corresponding to a large range of Reynolds and Froude numbers [12]. The present study focuses on experimental and numerical comparison for $D = 5\ cm$, with $15\,000 < Re < 60\,000$ and $0.4 < Fr < 1.7$, corresponding to the onset of air-entrainment. In the first part, the experimental setup is described. In the second part, the numerical method is presented. Then, in the final part, the numerical and experimental results are compared with each other. Specifically the drag forces measurements, the free-surface deformations and the evolution of the cavity depth $\mathcal{L}$ are highlighted.

2 Experimental method

The case study is a hollow cylinder in PMMA of 50 mm diameter. The cylinder is clogged at the end, attached vertically, perpendicularly to the water free-surface, and translated on a carriage riding horizontally along the flume of 34 m length, 90 cm width and 120 cm height. The experiment is shown schematically in figure 1(*a*). An acceleration protocol is applied to the cylinder : (i) the velocity increases linearly along a distance of 3.5 m, (ii) the speed is maintained constant over a distance of 9.5 m, where forces measurements are acquired in steady state, finally (iii) the speed decreases linearly in a distance of 2 m.

A window located on the sidewall of the flume, allows local flow visualisation around cylinder. The determination of the critical velocity at which air-entrainment occurs in the cylinder wake is based on images from a 2000 × 2000 pixels CCD camera (Basler aca2040) with focal length of 50 mm. A typical

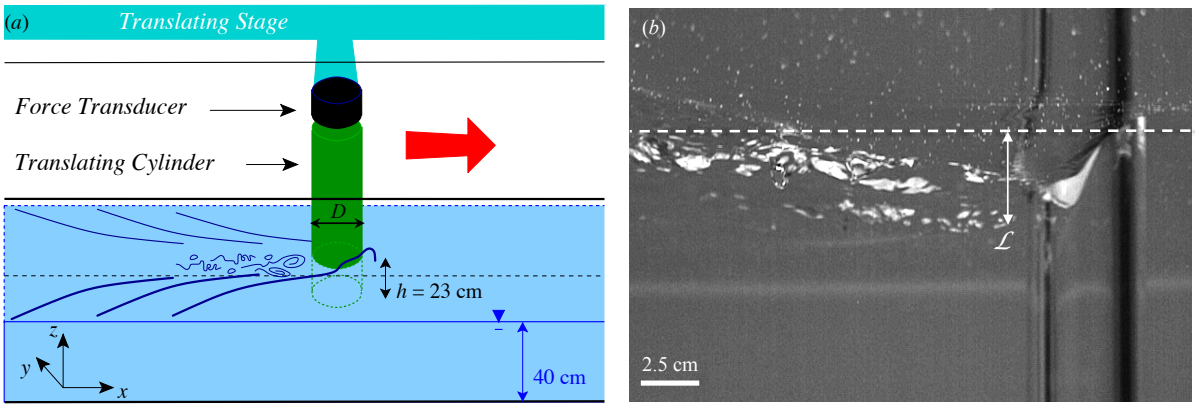

FIGURE 1 – Experimental setup. (a) schematic of the arrangement around the cylinder, view from the side above-surface. (b) Typical picture side view. The cylinder is translated from left to right with a velocity of 60 cm/s, $Re = 30\,000$ and $Fr = 0.86$. The depth of the cavity $\mathcal{L}$ is represented in the near cylinder wake.

image of the cylinder passing through the field of view of the camera is shown in figure 1(b). The working fluid is tap water and its height in the flume is constant at 40 ± 0.1 cm. The experiments were performed at constant immersion depth $h = 23 \pm 0.1$ cm leading to h/D of 4.6. The velocity range allows to reach $15\,000 < Re < 60\,000$ and $0.4 < Fr < 1.7$.

A piezoelectric sensor (Kistler 9327C), placed above the cylinder (see Figure 1(a)) measures the axial force, F_x, acting on the whole cylinder with a sensitivity of -7.8 pC/N. The sensor is connected to a charge amplifier equipped with a low pass filter of 30 Hz. The contribution of air drag is neglected. Indeed, the maximum error on C_D is about 0.2%. Force signals are acquired with a sample rate of 100 Hz. In order to measure the effect of air-entrainment on drag forces, a moving average on 20 points during 5 s on F_x at constant translating velocity was performed. The drag coefficient C_D can thus be defined using the formula :

$$C_D(t) = \frac{2\bar{F}_x}{\rho h D U^2}. \tag{1}$$

3 Numerical method

All the results presented below have been obtained with the YALES2 software which is briefly described hereafter. Then a specific focus is done on the level-set method which is used to treat the free surface. Finally, the numerical setup for the moving cylinder simulations are described in the last subsection.

3.1 Description of the YALES2 library

YALES2 [14] is a Computational Fluid Dynamics code that aims at solving the unsteady Navier-Stokes equations under the low-Mach number hypothesis on massively parallel computers. It is used and developed by more than 200 people at CORIA and in several laboratories. It is able to handle efficiently unstructured meshes with several billions of elements [15, 16], thus enabling the Direct Numerical Simulation (DNS) and Large-Eddy Simulation (LES) of laboratory and semi-industrial configurations. It is organised as a collection of solvers which gives the possibility to cover a wide range of phenomena and applications. Moreover, these solvers may be assembled to address multi-physics problems either directly or with some code coupling tools as OpenPALM [17]. YALES2 is based on the MPI-1 standard and is mostly written in Fortran 90 with some features of Fortran 2008 for the memory contiguity. The

low-Mach number Navier-Stokes equations are solved with a projection method for constant and variable density flows [18, 19]. These equations are discretised with a finite-volume 4th-order central scheme in space and a 4th-order Runge-Kutta like scheme in time [20]. The efficiency of projection approaches for low-Mach number flows is usually driven by the performances of the Poisson solver. In YALES2, the linear solver is a highly efficient Deflated Preconditioned Conjugate Gradient (DPCG) that has two mesh levels [21].

3.2 Treatment of free-surfaces in YALES2

To capture the free-surface, the generic front-tracking ACLS (Accurate Conservative Level Set) method [22] is used. This method is an improvement of the classical CLS method from [23] which enables to accurately predicts the interface dynamics while conserving the liquid mass. The principle of this algorithm is to transport a scalar ψ such that the interface Γ is located at $\psi = 0.5$.

$$\Gamma = \{x \in \mathbb{R}^3 | \psi(\mathbf{x}, t) = 0.5\} \tag{2}$$

In this method, the ψ scalar is imposed to have a hyperbolic tangent profile in the direction normal to the interface :

$$\psi(\mathbf{x}, t) = \frac{1}{2}\left(\tanh\left(\frac{\phi(\mathbf{x}, t)}{2\varepsilon}\right) + 1\right) \tag{3}$$

where 2ε is the thickness of the profile, and $\phi = \pm|\mathbf{x} - \mathbf{x}_\Gamma|$ is the signed-distance function. Assuming the flow velocity $\mathbf{u}$ is divergence free, the scalar ψ is first advected by the fluid :

$$\frac{\partial \psi}{\partial t} + \nabla \cdot (\psi \mathbf{u}) = 0 \tag{4}$$

and then reshaped using the reinitialization equation of Desjardins *et al.* [22] :

$$\frac{\partial \psi}{\partial \tau} = \nabla \cdot (\varepsilon (\mathbf{n} \cdot \nabla \psi) \mathbf{n} - \psi(1 - \psi)\mathbf{n}) \tag{5}$$

where τ is a pseudo-time, and $\mathbf{n} = \nabla\phi$ is the interface normal. This last step ensures that the ψ profile remains a hyperbolic tangent once convergence is achieved, i.e. $\frac{\partial \psi}{\partial \tau} = 0$.

The coupling of the two phases is ensured by the Ghost-Fluid Method (GFM) [24]. It consists in incorporating the pressure jump at the interface due to surface tension in the solving of the Poisson equation for the pressure that arises in the projection method. The GFM assumes that the jump condition for the pressure $[P]_\Gamma$ and its spatial derivatives $[\nabla P]_\Gamma$, $\left[\nabla^2 P\right]_\Gamma$, ...are known at the interface Γ. Then, the GFM is based on the extension by continuity of P_l in the gas and of P_g in the liquid. This extension allows to define the jump $[P]_\Gamma$ not only at the interface but also in the neighbourhood of the interface. In a one-dimensional domain with constant spacing, assuming that the interface Γ is located somewhere between $\mathbf{x}_i$ and $\mathbf{x}_{i+1}$ with the node i in the gas and the node $i+1$ in the liquid, and introducing the index $\theta = (\mathbf{x}_\Gamma - \mathbf{x}_i) / (\mathbf{x}_{i+1} - \mathbf{x}_i)$ and a modified density $\rho^\star = \rho_g\theta + \rho_l(1 - \theta)$, the pressure jump at $\mathbf{x}_{i+1}$ reads :

$$[P]_{i+1} \approx \frac{\rho_g}{\rho^\star}[P]_\Gamma + \left(1 - \frac{\rho_g}{\rho^\star}\right)(P_{l,i+1} - P_{g,i}) \tag{6}$$

and similar formula to obtain $[P]_i$. Finally, the pressure jump at the interface is given by [27] :

$$[P]_\Gamma = \sigma\kappa + 2[\mu]_\Gamma (\mathbf{n} \otimes \mathbf{n}) : \nabla\mathbf{u} \tag{7}$$

where σ is the surface tension between the two fluids, κ is the local interface curvature and the last term is usually a small correction due to the viscosity jump. An extension of this method to 3D unstructured meshes [25] has been implemented in the YALES2 solver.

3.3 Numerical setup for the simulation

As the cylinder is moving with a constant velocity with respect to the flume, the simulations can be performed in the reference frame attached to the cylinder without further modelling. All the walls of the flume are considered as walls moving with the velocity of the cylinder but in opposite direction, which is identical to the inlet velocity. On the other hand, the cylinder walls are treated with a classical no-slip boundary condition. The initial mesh contained 1.7 millions tetrahedral cells and a mesh convergence study was performed to ensure mesh independence of the results. The final mesh contains 47.9 million tetrahedral cells, the edges of the elements are set to 2.5 mm on the cylinder wall and to 5 mm inside the flume with a growth rate of 1.1. The domain and boundary conditions are depicted on figure 2.

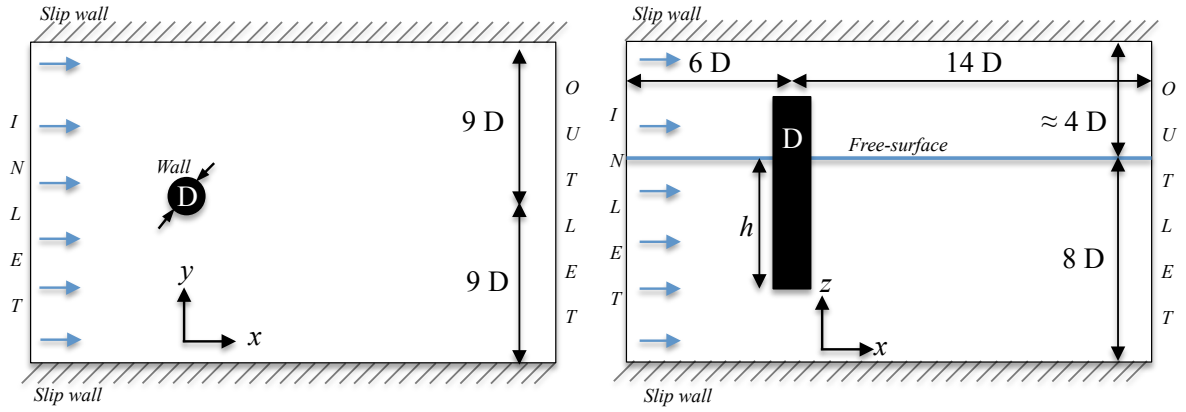

FIGURE 2 – Domain and boundary conditions. Top view and side view of the numerical domain.

The flow in the wake of the cylinder is fully turbulent and the mesh size in this zone is not fine enough to capture the smallest eddies : the Large-Eddy Simulation (LES) formalism is thus used to take into account the sub-grid scale contributions. The WALE [28] turbulence model was used in the present simulations.

The time-step of the simulation is computed by setting both a CFL and a surface tension stability constraint. The first one imposes that for any pair of nodes i and j :

$$\frac{\mathbf{u}_{ij} \cdot \mathbf{A}_{ij} \Delta t_{\mathrm{CFL}}}{V_i} < \mathrm{CFL}_{\max} \tag{8}$$

where V_i is the volume of the control-volume i while $\mathbf{A}_{ij}$ refers to the control-volume boundary element between nodes i and j and $\mathbf{u}_{ij}$ is the fluid velocity on this boundary element. On the other hand, the surface tension stability constraint is also written for each pair of nodes i and j as :

$$\sqrt{\frac{\sigma|\kappa_{ij}|}{\rho_g}} \frac{\Delta t_{\mathrm{ST}}}{\Delta_{ij}} < \mathrm{ST}_{\max} \tag{9}$$

where κ_{ij} is the local curvature of the interface while Δ_{ij} is the length of the pair.

In the present simulation $\mathrm{CFL}_{\max} = 0.9$ and $\mathrm{ST}_{\max} = 0.5$ which gives $\Delta t_{\mathrm{CFL}} \approx 1.0\,\mathrm{ms}$ (for the

simulation at the highest Reynolds number) and $\Delta t_{\mathrm{ST}} \approx 0.2\,\mathrm{ms}$ (identical for all the simulations). In all cases, it was found that the time-step was always limited by the surface tension constraint.

All the simulations were performed on 840 Intel Broadwell E5-2680 v4 cores of the Myria supercomputer from CRIANN [26]. Each simulation was conducted for 5 s of physical time which was achieved in approximately 15 hours of Wall-Clock Time. This accounts for around 12 600 CPU.h for each simulation.

All the statistics that are presented in the next sections were gathered during a physical time of $\tau_{stats} = 1s$, after having performed 4 s to eliminate the transient initial state. This time can be compared to the characteristic timescale based on the cylinder velocity and diameter $\tau_{\mathrm{cyl}} = D/U$. The number of flow through times $N_{flow} = \tau_{stats}/\tau_{\mathrm{cyl}}$ thus depends on the Reynolds number : $N_{flow}(Re = 60\,000) \approx 24$ for the highest studied Reynolds number while $N_{flow}(Re = 15\,000) \approx 6$ for the lowest one. In all the cases, the statistics were performed with a sampling rate of 100 Hz.

4 Drag and air-entrainment

In this section, force measurements are performed in a range of Re and Fr, such that the transition to air-entrainment is observed. Figure 3 presents drag coefficients measurements as a function of Re obtained by experiments and simulations. Filled symbols correspond to cases without air-entrainment while empty symbols refers to air-entrainment in the cavity behind the cylinder. The error bars correspond to the standard deviation of C_D. In either case, the drag coefficient first increases with the Re then decreases after air-entrainment occurred in the cavity.

This cavity $\mathcal{L}$ [6, 7] forms viscous cusps where air-entrainment is systematically injected. Air-entrainment in the cavity is defined when the first bubble is observed along the cylinder wall. Once air bubbles are injected into the flow, they are carried downstream into the wake. The onset of air-entrainment in the cavity $\mathcal{L}$ has been observed experimentally (see Figure 3(*b*)) and numerically (see Figure 3(*c*)). The transition toward air-entrainment in the cavity occurs at similar $Re \simeq 40\,700$ for experiments and $Re \simeq 40\,000$ for numerics.

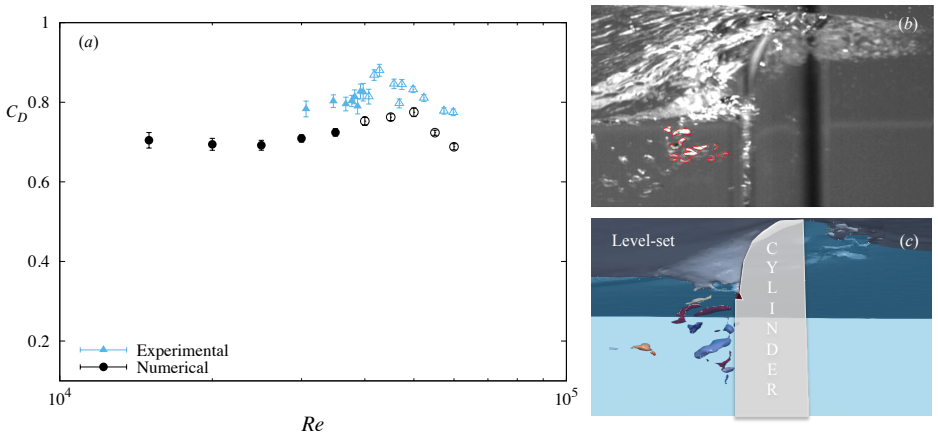

FIGURE 3 – (*a*) C_D as a function of Re at constant $h = 23 \pm 0.1$ cm. Filled symbols represent situation without air-entrainment and empty symbols represent flow with air-entrainment in the cavity. (*b*) Experiments: Air-entrainment in the cavity behind the cylinder at $Re = 45\,680$ and $Fr = 1.3$, bubbles encircled in red, (*c*) Numerics: Air-entrainment in the cavity behind the cylinder at $Re = 60\,000$ or $Fr = 1.7$, bubbles are represented in colours.

5 Free-surface deformations

In order to inspect the free-surface elevation, the time-averaged free-surface during $\tau_{stats} = 1$ s is depicted in figure 4 for three different $Fr = 0.86$, 1.29, and 1.71 corresponding to $Re = 30\,000$, 45 000 and 60 000. For the three cases, the bow wave in front of the cylinder, the cavity region downstream the cylinder, and the Kelvin waves are observed.

For $Re = 30\,000$, and $Fr = 0.86$, the Kelvin waves [7, 1] have a wavelength of $\lambda/D = 2\pi Fr^2$, i.e. $\lambda/D \simeq 4.6$. For highest Fr, $\lambda/D \simeq 10.5$ and 18.4, the numerical domain is too narrow to observed these wavelengths. Concerning the Kelvin angles, a linear decrease of the angle from almost 55° at $Fr = 0.86$ to 43° at $Fr = 1.71$ is obtained. These results are in agreement with numerical simulations performed by Koo [7] at similar Fr.

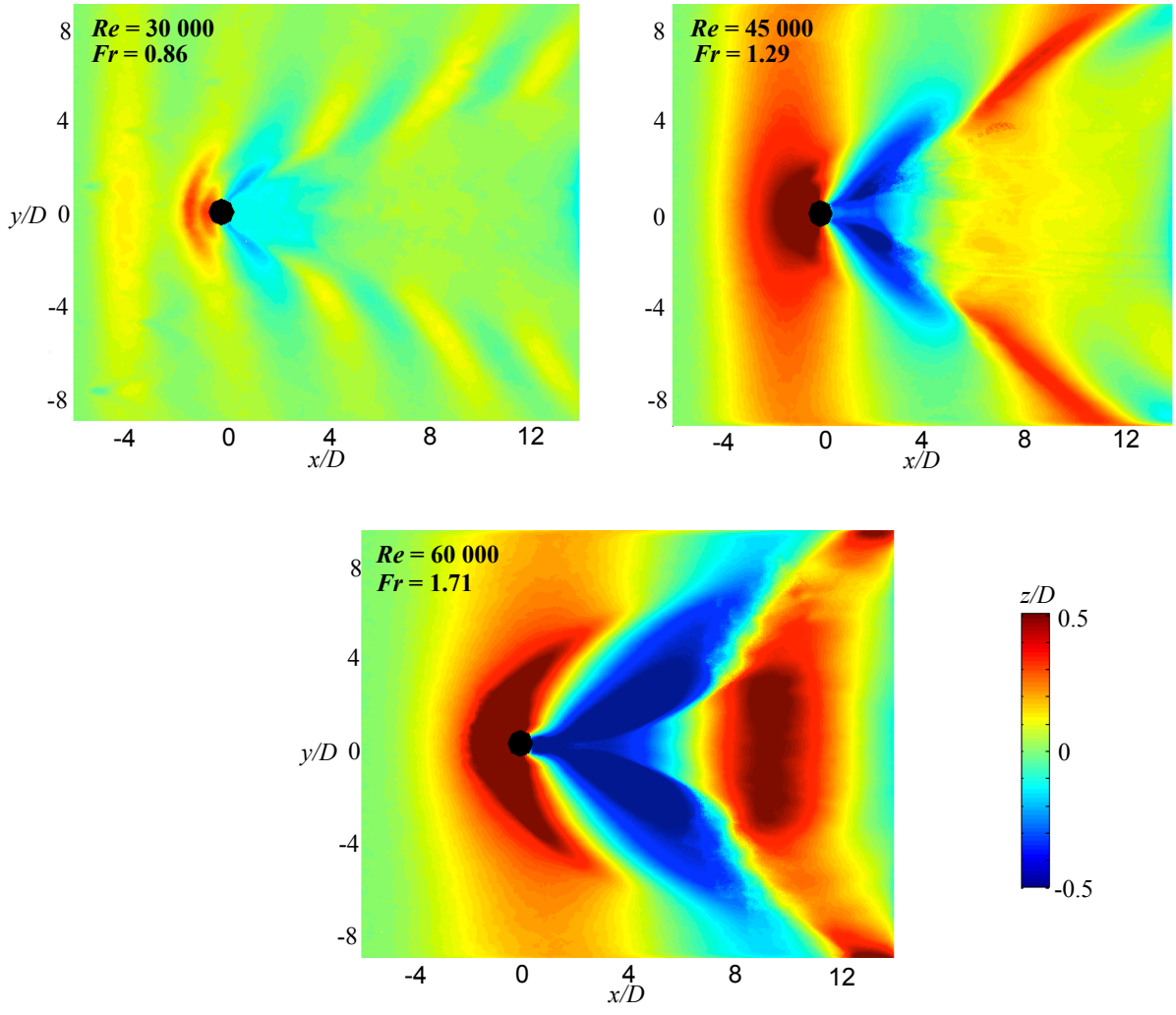

FIGURE 4 – Colormap of time-averaged free-surface elevation for three different Re and Fr obtained from numerical simulations. The axes and the elevation are made dimensionless using D.

Downstream of the cylinder the cavity forms and increases with Fr. The evolution of the cavity $\mathcal{L}$ is obtained from experiments and simulations. Experimentally, the measurements of the cavity depth $\mathcal{L}$ are gathered from direct observations of graduated cylinder (see Figure 5(b)). $\mathcal{L}$ represents the mean value from 10 snapshots. The error bars are the maximum observed deviation. Numerically, $\mathcal{L}$ is defined in

figure 4 at the position $y/D = 0$. The error bars provided from the standard deviation.

The cavity depth evolution $\mathcal{L}/D$ achieved by experiments and simulations, is described in figure 5(a) as a function of Fr^2Re. A linear evolution is observed in both cases before air-entrainment occured in the cavity, which is consistent with the equation (10) proposed by Benusiglio [11].

$$\mathcal{L}/D \propto \frac{U^3}{g\nu} \propto Fr^2Re, \tag{10}$$

For larger values of Fr^2Re corresponding to air-entrainment in the cavity, the evolution becomes non-linear.

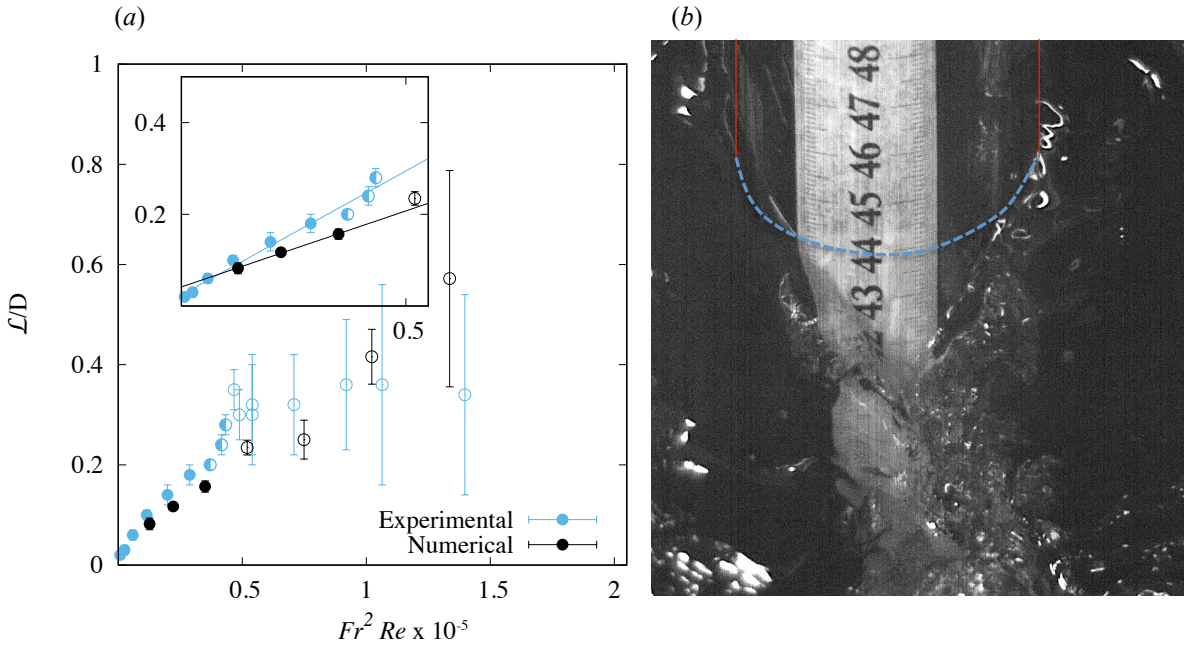

FIGURE 5 – (a) Non-dimensional cavity depth $\mathcal{L}/D$, as a function of Fr^2Re. The partially filled symbols correspond to air-entrainment in the wake. The inset is a zoom restricted to the regime of no or wake air-entrainment, where the continuous lines are linear fits. (b) is a snapshot of the cavity view, from the back, at Re = 50 000. The continuous vertical red lines represent the emerged cylinder walls and the dashed blue line represents the free-surface at rest.

6 Conclusion

Experimental and numerical results on the flow dynamics around a vertical translating cylinder of diameter 5 cm in water have been presented. The focus was on drag force measurements, free-surface elevation, and critical velocity for air-entrainment. A good agreement between experiments and simulations was obtained for the cavity depth, the drag coefficient and the critical velocity. It is planned to extend this study to other diameters in the near future.

As a perspective, the YALES2 numerical tool is able to perform some topology analysis to distinguish between the liquid phase and the gaseous inclusions : this kind of analysis will be applied in a near future to assess the size of the bubbles in the wake of the cylinder. Another interesting extension would be to

use some adaptative mesh refinement [29] to improve the description of the free-surface dynamics in the near-wake region while keeping the CPU cost reasonable.

Références

[1] Rabaud, M. and Moisy, F., *Ship wakes*: *Kelvin or Mach angle*?, Phys. Rev. Lett., 110(21) (2013) 214503

[2] López, I., Andreu, J.,Ceballos, S., de Alegría, I. M. and Kortabarria, I., *Review of wave energy technologies and the necessary power-equipment*, Rene. Sust. Energy Revi., 27 (2013) 413–434

[3] Schewe, G., *On the force fluctuations acting on a circular cylinder in crossflow from subcritical up to transcritical Reynolds numbers*, J. Fluid Mech., 133 :265-285 (1983)

[4] D. J. Tritton, *Experiments on the flow past a circular cylinder at low Reynolds numbers*, J. Fluid Mech., 6(04) (1959) 547–567

[5] Breuer M., *A challenging test case for large eddy simulation : high Reynolds number circular cylinder flow*, Inter. J. Heat Fluid Flow, 21(5) (2000) 648–654

[6] Yu, G., Avital, E. J. and Williams, J. J., *Large eddy simulation of flow past free surface piercing circular cylinders*, J. Fluids Eng., 130(10) (2008) 101304-2

[7] Koo, B.,Yang, J., Yeon, S. M. and Stern, F., *Reynolds and Froude number effect on the flow past an interface-piercing circular cylinder*, Int. J. Nav. Archit. Ocean Eng., 6(3) (2014) 529–561

[8] Chaplin, J. R. and Teigen, P., *Steady flow past a vertical surface-piercing circular cylinder*, J. Fluids Struct., 18(3) (2003) 271–285

[9] Ducrocq, T., Cassan, L., Chorda, J. and Roux, H., *Flow and drag force around a free surface piercing cylinder for environmental applications*, Environ. Fluid Mech., 17 (2017) 629–645

[10] Keough, S. J., Kermonde, I. L., Amiet, A., Philip, J., Ooi, A., Monty, J. P. and Anderson, B., *Time resolved measurements of wake characteristics from vertical surface-piercing circular cylinders*, 20th Australian Fluid Mechanics Conference, (2016)

[11] Benusiglio, A., *Indiscrétions aux interfaces*, Thèse Ecole Polytechnique, (2013)

[12] Ageorges, V., Peixinho, J., & Perret, G., *Flow and air-entrainment around partially submerged vertical cylinders*, Bulletin of the American Physical Society, (2018)

[13] Moisy, F. and Rabaud, M., *Mach-like capillary-gravity wakes*, Phys. Rev. E, 90(2) (2014) 023009

[14] Moureau, V. and Lartigue, G., *http ://www.coria-cfd.fr*, YALES2

[15] Moureau, V., Domingo, P., & Vervisch, L., *Design of a massively parallel CFD code for complex geometries*, Comptes Rendus Mécanique, 339 :2-3 (2011) 141–148

[16] Moureau, V., Domingo, P., & Vervisch, L., *From Large-Eddy Simulation to Direct Numerical Simulation of a lean premixed swirl flame : Filtered laminar flame-PDF modeling*, Comb. and Flame, 158(7) (2011) 1340–1357

[17] Duchaine, F., Maheu, N., Moureau, V., Balarac, G., & Moreau, S., *Large-Eddy Simulation and conjugate heat transfer around a low-mach turbine blade*, J. Turbomach., 136(5) (2013)

[18] Chorin, A. J. *Numerical Solution of the Navier-Stokes Equations*, Mathematics of computation, 22 (1968) 745–762

[19] Pierce, C.D., and Moin, P., *Progress-variable approach for large eddy simulation of non-premixed turbulent combustion*, J. Fluid Mech., 504 (2004) 73–97

[20] Kraushaar, M., *Application of the compressible and low-mach number approaches to large-eddy simulation of turbulent flows in aero-engines*, Thèse Institut National Polytechnique de Toulouse, 2011

[21] Malandain, M., Maheu, N., & Moureau V., *Optimization of the deflated Conjugate Gradient algorithm for the solving of elliptic equations on massively parallel machines*, J. Comp. Phys., 238 (2013) 32–47

[22] Desjardins, O., Moureau, V., & Pitsch, H., *An accurate conservative level set/ghost fluid method for simulating turbulent atomization*, J Comp. Phys., 227 (2008) 8395–8416

[23] Olsson, E., and Kreiss, G., *A conservative level set method for two phase flow*, J Comp. Phys., 210 (2005) 225–246

[24] Fedkiw, R., Aslam, T., Merriman, B., & Osher, S., *A non-oscillatory Eulerian approach to interfaces in multimaterial flows (the ghost fluid method)*, J. Comput. Phys., 152(2) (1999) 457–492

[25] Luo, H., Baum, J., & Lohner, R., *An improved finite volume scheme for compressible flows on unstructured grids*, American Institute of Aeronautics and Astronautics, 33 (1995)

[26] https ://www.criann.fr/

[27] Delhaye, J.M. *Jump conditions and entropy sources in two phase systems. Local instant formulation*, Int. J. Multiphase Flow, 1(3) (1974) 395–409

[28] Ducros, F., Nicoud, F., & Poinsot, T. *Wall-Adaptating Local Eddy-Viscosity models for simulations in complex geometries*, Numerical Methods for Fluid Dynamics, 6 (1998) 293–299

[29] Leparoux, J., Mercier, R., Moureau, V., & Musaefendic, H., *Primary atomization simulation applied to a jet in crossflow aeronautical injector with dynamic mesh adaptation*, 14th Triennal International Conference on Liquid Atomization and Spray Systems, 2018